ACS APPLIED ENERGY MATERIALS
Cite This: ACS Appl. Energy Mater. 2019, 2, 8274−8282
Article
www.acsaem.org

Ag−TiO_2 Hybrid Nanocrystal Photocatalyst: Hydrogen Evolution under UV Irradiation but Not under Visible-Light Irradiation

Shelton J. P. Varapragasam,[†,∥] Shahzahan Mia,[†,∥] Carly Wieting,[†] Choumini Balasanthiran,[‡] Md Yeathad Hossan,[†] Aravind Baride,[†] Robert M. Rioux,*[,‡,§] and James D. Hoefelmeyer*[,†]

[†]Department of Chemistry, University of South Dakota, 414 East Clark Street, Vermillion, South Dakota 57069, United States
[‡]Department of Chemical Engineering and [§]Department of Chemistry, The Pennsylvania State University, 22 Chemical Biomedical Engineering Building, University Park, Pennsylvania 16802-4400, United States

Supporting Information

ABSTRACT: We report a thermolytic reduction of silver precursors in the presence of anatase TiO_2 nanorods to form Ag−TiO_2 hybrid nanocrystals (HNCs). Upon changing the reaction conditions, the size and number density of Ag on the HNCs could be adjusted. The size and number density of Ag on the HNCs were found to have an inverse relation. We assess the hydrogen evolution of TiO_2 nanorods, P25 TiO_2, and Ag−TiO_2 HNCs in methanol/water under xenon lamp irradiation. The turnover frequency for hydrogen evolution on silica-supported Ag−TiO_2 was 1.4×10^{-4} s^{-1}, greater than that of the anatase TiO_2 nanorods (9.8×10^{-6} s^{-1}) or the coupled anatase/rutile TiO_2 (P25 catalyst; 5.2×10^{-5} s^{-1}).

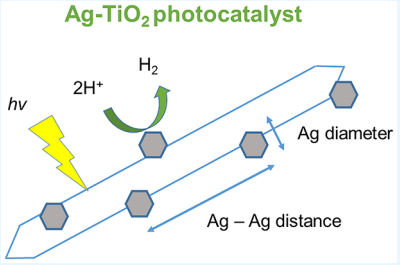

KEYWORDS: *nanocrystal, TiO_2, silver, hydrogen, photocatalysis*

INTRODUCTION

Semiconductor photocatalysis, particularly for the purpose of artificial photosynthesis-type[1−3] reactions such as water splitting, has attracted intense interest because the concept offers the possibility of addressing pressing global issues through utilizing solar energy.[4−7] The semiconductor photocatalysis scheme involves light absorption by the semiconductor that increases the population of conduction band electrons and valence band holes, followed by electron-transfer reactions at the semiconductor interface.[8,9] The efficiency of the process is limited by the undesired fates of the excited electron/hole pair, the efficiency of light absorption, and the stability of the photocatalyst. For widespread applications, the material must have a high benefit/cost ratio, which favors active catalysts composed of stable, nontoxic, earth-abundant materials that are easy to prepare. Overcoming these limitations is the principal driver in the research of new materials and the light-activated processes that occur within them.

The introduction of a metal particle on the surface of a semiconductor can contribute multiple advantages to the photocatalysis process:[10] (1) On the basis of the energy difference between the metal Fermi level and the semiconductor band-edge potential, the photoexcited electrons and holes can be separated among the two material phases. (2) The metal surface can promote the electron-transfer reaction with substrates and enable faster catalysis. Additional possibilities exist for plasmonic metal particles:[11,12] (3) The plasmonic metal could be tuned to absorb photons over an energy range not absorbed by the semiconductor. (4) The localized electric field due to the excited surface plasmon can lead to electron transfer from the metal to the semiconductor conduction band. Whereas the metal−semiconductor junction can facilitate the separation of electrons and holes, the direction of electron flow depends on the excitation mechanism, whether it is semiconductor band-gap excitation or metal plasmon excitation. In the former, there is fast transfer of the photoexcited electron from the semiconductor to the metal. For example, the transfer of photoexcited electrons from CdS to Au occurs on a sub-20 fs time scale in metal−semiconductor matchstick hybrid nanocrystals.[13] Conversely, in metal−semiconductor hybrid nanocrystals in which the metal has strong surface plasmon resonance (SPR), the excitation of the surface plasmon produces a strong near-field effect with electron transfer from the metal to the semiconductor conduction band.[14−18] This effect is strongly dependent on the metal particle size and shape.[19] For example Au−TiO_2 heterostructures with different Au nanoparticle sizes (4 and 67 nm) were prepared and found to exhibit distinct charge-separation mechanisms upon light excitation.[20] The 4 nm Au nanoparticles have weak SPR with charge transfer occurring upon band-gap excitation of TiO_2, followed by conduction band electron transfer to Au, whereas, 67 nm Au nanoparticles with strong SPR donate electrons to the TiO_2 conduction band upon the excitation of the metal plasmon.

The control of the material morphology on the nanoscale affords the ability to tune the electronic structure and surface properties of materials and enables the possibility of highly

Received: September 4, 2019
Accepted: October 31, 2019
Published: November 12, 2019

DOI: 10.1021/acsaem.9b01730
ACS Appl. Energy Mater. 2019, 2, 8274−8282

engineered nanostructured materials for efficient photocatalysis. With this impetus, examples and design strategies of well-defined hybrid nanocrystal (or heteronanocrystal) (HNC) structures are on the rise. HNCs combine physicochemical and optoelectronic properties of the component crystal phases as well as emergent features upon the combination of the crystal phases in selected orientations and spatial combinations.[21−26] Whereas the concept of colloidal photoelectrochemical catalysts dates back several decades,[27] rapid advances in instrumentation and synthesis methods for nanocrystals have led to several well-defined metal−semiconductor HNCs.[28−40] Most examples utilize rod-shape semiconductor nanocrystals to take advantage of the longitudinal electron delocalization for charge separation in the HNC.[41] Recent work from the Amirav group indicate that fewer metal cocatalyst domains on the semiconductor nanocrystal lead to a higher rate of photocatalysis,[42] and the cocatalyst size plays an important role.[43] Thus the design principles for metal−semiconductor HNC photocatalysts are improving at a rapid pace.

We are interested in the study of Ag−TiO_2 HNCs as a photocatalyst for hydrogen evolution. Several Ag−TiO_2 nanostructures,[44,45] including HNCs, have been reported as photocatalytic materials. From these studies, there is increasing knowledge of the factors that influence the role of Ag as an electron sink or plasmonic sensitizer. For example, Ag−TiO_2 HNCs with a high number density of Ag nanoparticles on the TiO_2 surface can give rise to interparticle coupling of the surface plasmon. In particular, Ag−TiO_2 HNCs in which rod-shape TiO_2 nanocrystals are multiply decorated with Ag nanoparticles give SPR absorbance spectra that mimic the SPR features of Ag nanorods, showing red-shifted longitudinal SPR modes.[46−49] This feature, in combination with changes in SPR due to the size and shape of the Ag nanoparticles, allows multiple avenues to change the light absorption properties of the Ag−TiO_2 HNCs. However, few studies report Ag SPR-sensitized photocatalysis,[50] and there is no putative evidence of this mechanism in Ag−TiO_2 HNCs.

There is considerable evidence that the band-gap irradiation of Ag−TiO_2 HNCs leads to electron accumulation in the Ag nanoparticles. Evidence of electron buildup was observed upon the irradiation of Ag/TiO_2 core−shell nanocrystals with UV light that led to a dynamic blue shift of the Ag SPR feature.[51] This effect could be produced with chemical reducing agents as well, and the addition of $NaBH_4$ to Ag−TiO_2 nanorods led to a significant blue shift in the Ag SPR without a change in the Ag nanoparticle size.[52] In addition, the UV irradiation of TiO_2 nanocrystals in contact with solutions of Ag^+ is an established method for the preparation of Ag−TiO_2 HNCs.[49−53] Initially, Ag nanoparticles nucleate on the TiO_2 nanocrystals at multiple locations on each nanocrystal. Over time, the Ag nanoparticle size grows with increasing irradiation. Eventually, the Ag particles undergo ripening to form HNCs with one Ag nanoparticle. The mechanism for ripening involves dissolution of the surface Ag^+ ions from smaller particles and deposition on the larger particles. In air and under visible-light irradiation, Ag−TiO_2 HNCs undergo oxidation of the silver domains with a total loss of the SPR given sufficient time, which could be restored upon the photoreduction of the Ag^+ under UV irradiation.[49] From these studies, the role of oxygen in etching and the formation/dissolution of Ag in the HNCs is well-established.

In this work, we prepare Ag−TiO_2 HNCs upon the chemical reduction of Ag^+ in the presence of rod-shaped TiO_2 nanocrystals and evaluate hydrogen evolution photocatalysis in water−methanol solutions. The Ag−TiO_2 HNCs show activity up to 12.3 μmol/g catalyst/min and an apparent quantum yield of 0.92% for hydrogen evolution under Xe lamp irradiation, from which the activity is derived from the incident UV radiation. Under visible-light illumination in which the Ag SPR is excited, we do not observe hydrogen evolution from water−methanol or water−formaldehyde solutions.

EXPERIMENTAL SECTION

Chemicals and Equipment. 1-Octadecene, (technical grade, 90%, Acros), oleic acid (90%, Fisher Scientific), oleylamine (>50%, TCI America), 1,2-hexadecanediol (technical grade 90%, Aldrich), TiO_2 (Aeroxide P25, ACROS Organics), $AgNO_3$ (99%, VWR), and methanol (99.9%, HPLC grade, 0.2 μm filtered, Fisher Scientific) were used. TiO_2 nanorods and Ag−TiO_2 HNCs were synthesized under a flow of N_2 with an in-line drying tower charged with P_2O_5. Sonication procedures utilized a Neytech 28H Ultrasonik (100 W, 44−48 kHz) sonication bath. Vortex mixing was achieved with a Vornado benchtop vortex mixer. Calcinations utilized an MTI KSL-1100X furnace. Centrifugation protocols utilized benchtop Thermo IEC Centra CL-2 or Eppendorf 5804 models configured to accept Falcon 50 mL conical centrifuge tubes.

Instrumentation. Transmission electron microscopy (TEM) images were obtained from a Tecnai Spirit G^2 Twin TEM (FEI Company) with a LaB_6 filament operating at 120 kV. HR-TEM images were obtained from a Titan G2 XFEG TEM operating at 200 kV. Scanning electron microscopy (SEM) data were obtained from a Zeiss Sigma FE-SEM with Oxford AZtec energy-dispersive X-ray spectroscopy (EDS) detector. Powder X-ray diffraction (PXRD) data were obtained from a Rigaku Ultima IV instrument. The X-ray tube produced Cu Kα radiation (λ = 1.54 Å), and the generator was set to 44 kV and 44 mA during data collection. Data refinement and analysis were performed with PDXL software. A Cary 50 spectrophotometer was used to obtain UV−vis absorption spectra of nanocrystal dispersions in hexanes. Photoluminescence spectra were obtained using a Fluoromax 4 spectrofluorometer. Hydrogen generation in the headspace of the photochemical reactor was measured by gas chromatography (GC) using an Agilent 7890A GC equipped with a 30 m × 320 μm column with 5 Å molecular sieves and Ar as the carrier gas.

Synthesis of TiO_2 Nanorods. Anatase-phase rod-shaped TiO_2 nanocrystals were prepared according to the procedure reported by the Hyeon group.[54] Degassed oleic acid and titanium isopropoxide were heated under inert conditions at 270 °C and kept for 2 h. The reaction mixture was cooled, isopropanol was added, and the product was precipitated after centrifugation at 3500 rpm for 8 min.

Synthesis of Hybrid Ag−TiO_2 HNCs. The synthesis of Ag metal hybrid TiO_2 nanorods was inspired by the method reported by Bigall and coworkers for noble-metal growth on CdSe nanoplatelets.[55] In this synthesis, 0.058 g (0.73 mmol) of TiO_2 nanorods, 0.124 g (0.73 mmol) of $AgNO_3$, 2.4 mL of oleylamine (7.29 mmol), 2.3 mL of oleic acid (7.29 mmol), 0.472 g of 1,2-hexadecanediol (1.83 mmol), and 20 mL of 1-octadecene were combined within a 100 mL three-necked flask. Volatiles were removed under vacuum at 50 °C over 20 min. Then, the flask was filled with N_2 and heated to 100 °C for 2.5 h. The reaction mixture was allowed to cool, and the product was separated by the addition of isopropanol, followed by centrifugation at 3500 rpm for 8 min, after which the supernatant was decanted. The precipitate was redispersed in hexanes.

Preparation of Supported Catalysts: TiO_2/SiO_2 and Ag−TiO_2/SiO_2. A slurry of 0.667 g fumed silica with 40 mL of hexanes was prepared in a 50 mL centrifuge tube. The contents were agitated with a vortex mixer for 2 min. Then, 20 mg of photocatalyst (TiO_2 or Ag−TiO_2) dispersed in hexanes was added to the centrifuge tube and sonicated for 20 min. After that, the contents were centrifuged at 3500

DOI: 10.1021/acsaem.9b01730
ACS Appl. Energy Mater. 2019, 2, 8274−8282

rpm for 8 min, and the clear supernatant was discarded. The uptake of TiO_2 on the SiO_2 surface was verified by UV−visible spectroscopy (Figure S1). The gelatinous precipitate of Ag−TiO_2/SiO_2 was spread onto a watch glass and dried under vacuum (~30 mTorr) at 175 °C for 24 h. The sample was allowed to cool to room temperature and was ground with a mortar and pestle.

Photocatalytic Hydrogen Evolution. A 150 mL quartz flask with a magnetic stirrer was charged with 10 mL of water, 2 mL of methanol, and catalyst (P25 or TiO_2 nanorod powder = 20 mg, silica-supported catalysts = 167 mg). The flask was sealed with a rubber septum and fitted with a 2.5 in. 20 gauge needle outlet. Argon gas (~50 sccm) was introduced to the flask through a needle to purge the contents for 30 min; then, the inlet and outlet needles were removed. Using a gastight syringe, a 1 mL aliquot of the headspace was extracted and injected into the GC, at which time no oxygen was detected. The flask was irradiated with a 150 W Xe Arc lamp powered by an ABET Technologies solar simulator. The photocatalytic reactor was covered with a wooden shield box to isolate the system from the outside light as well as to avoid UV-light exposure. The headspace was sampled at desired time intervals for GC analysis. In a separate control experiment, a mixture containing two supported catalysts (83.4 mg of calcined Ag nanoparticles supported on SiO_2 (1.5% Ag) and 83.4 mg of calcined TiO_2 nanorods supported on SiO_2 (1.5% TiO_2)) was evaluated.

RESULTS AND DISCUSSION

Synthesis and Characterization. Oleic-acid-stabilized anatase TiO_2 nanorods were prepared according to the procedure reported by Hyeon.[54] From this protocol, we routinely obtained multigram quantities of nanocrystals. PXRD and TEM data from the samples are shown in Figure 1. PXRD data indicate the presence of the anatase TiO_2 phase. The (004) reflection shows a higher relative intensity and narrower line width, which are indicators of the anisotropic nature of the nanocrystal due to the selective growth in the [001] direction. The Rietveld analysis of the data indicated that anatase was phase pure and the crystallinity was 96%. The refinement indicated a crystallite of 10.7 nm, whereas the size calculation from the Williamson−Hall method indicated a crystallite of 3.2 nm. The discrepancy is likely due to the highly anisotropic nature of the anatase nanorods. We note that the Williamson−Hall result is consistent with the diameter of the nanocrystal. Unfortunately, because of the systematic absences of (00*l*) reflections, there are too few diffraction peaks for the calculation of the crystallite size in the *c* direction. A Debye−Scherrer analysis of the (004) reflection yields a crystallite of 17.7(9) nm. TEM data indicate nanorods with an average length of 42.0 ± 7.3 nm and a diameter of 3.1 ± 0.4 nm. From HRTEM data, we observe lattice fringes consistent with the distance and orientations from the {101} and (004) planes. The (004) planes are oriented perpendicular to the major axis of the nanorod, confirming the growth of the crystal in the [001] direction. The bulk analysis from PXRD data is in good agreement with TEM data.

Dispersions of TiO_2 nanorods in 1-octadecene were heated to 100 °C with $AgNO_3$, oleic acid, oleylamine, and 1,2-hexadecanediol. The initial dispersion changed color from light straw to dark brown over time as the silver ion was reduced. The addition of isopropanol to the reaction mixture led to a floc that was subjected to centrifugation. The supernatant was discarded, and the dark-brown solids were redispersed in hexanes to give a stable dispersion of Ag−TiO_2 HNCs.

In the reaction, oleylamine and 1,2-hexadecanediol contribute to the reduction of the Ag^+ ion and the formation of Ag nanoparticles. The use of 1,2-hexadecanediol (without oleylamine) led to the formation of Ag nanoparticles with an average diameter of 1.9 ± 0.7 nm, and the nanoparticles were

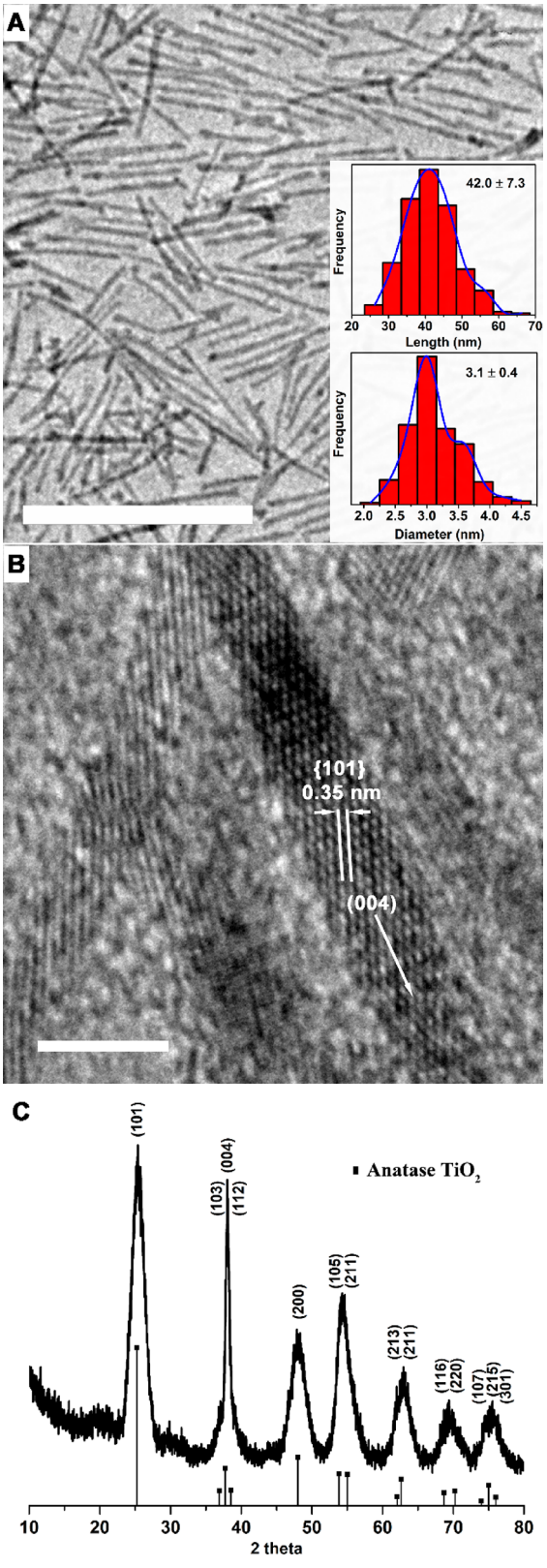

Figure 1. (A) TEM image of the TiO_2 nanorods with length and diameter histograms (scale bar = 100 nm). (B) HRTEM image of the TiO_2 nanorods (scale bar = 5 nm). (C) Powder X-ray diffraction data and relative intensity lines of anatase TiO_2 from JCPDS no. 00-021-1272.

DOI: 10.1021/acsaem.9b01730
ACS Appl. Energy Mater. 2019, 2, 8274−8282

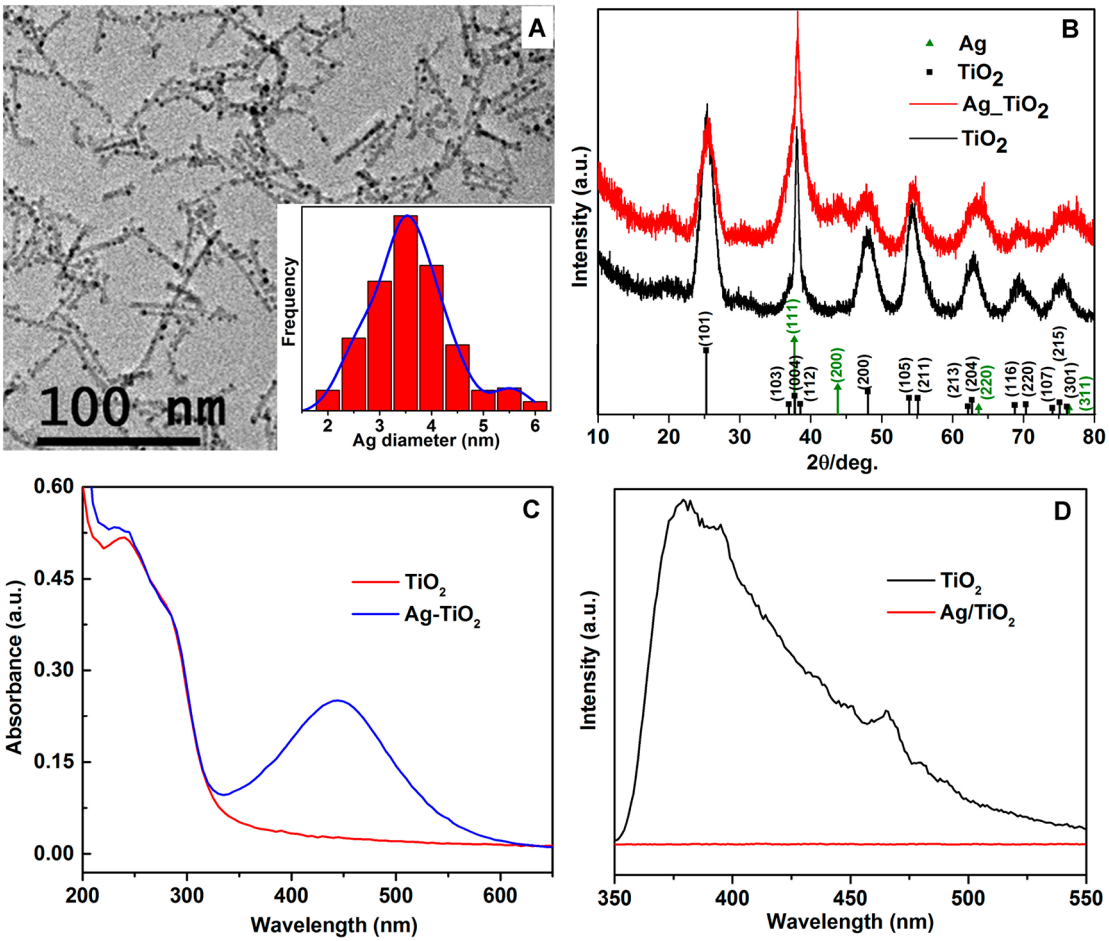

Figure 2. Ag−TiO_2 HNCs prepared from 4:1 oleylamine/1,2-hexadecanediol reducing agent and a 1:1 ratio of Ag/TiO_2 in the reaction. (a) TEM image and size distribution of Ag nanoparticles, (b) powder X-ray diffraction patterns, (c) UV−visible absorption spectra, and (d) photoluminescence emission spectra (λ_{ex} = 300 nm) of TiO_2 nanorods and Ag−TiO_2 HNCs.

not attached to TiO_2 (Figure S2), whereas the use of oleylamine (without 1,2-hexadecanediol) led to Ag−TiO_2 HNCs with a Ag nanoparticle average diameter of 1.4 ± 0.5 nm (Figure S3). In this case, the HNCs were multiply decorated with Ag nanoparticles. We found the combination of oleylamine/1,2-hexadecanediol in a 4:1 ratio as the reducing agent led to the growth of Ag nanoparticles on the surface of the TiO_2 nanorods with an average diameter of 3.4 ± 0.8 nm (Figure 2a and Figure S4). In all of the reactions, the size and shape of the TiO_2 nanorods were retained. PXRD data from Ag−TiO_2 HNCs (shown in Figure 2b) indicated the presence of anatase TiO_2 (versus JCPDS no. 00-021-1272) and fcc Ag phases (versus JCPDS no. 00-004-0783). Rietveld and reference intensity ratio (RIR) analyses of the data indicated Ag and anatase TiO_2 phases in a 29:71% ratio. The Ag and TiO_2 crystallites were calculated as 1.5 and 4.1 nm, respectively, from the Williamson−Hall method. As previously discussed, the calculated crystallite size of TiO_2 is representative of the nanorod diameter, whereas the narrow line width and increased relative intensity of the anatase (004) reflection indicate a highly anisotropic nanocrystal. SEM and EDS of the Ag−TiO_2 sample (Figure S5) indicate a uniform distribution of Ti and Ag on the micron scale with a consistent ratio of Ag/Ti 25:75% over multiple regions. The EDS result is in close agreement with the Ag/TiO_2 phase ratio from the PXRD data analysis. The UV−visible absorption spectrum obtained from a dilute dispersion of Ag−TiO_2 HNCs shows two main features (Figure 2c). Below 300 nm, there is strong absorbance due to O 2p → Ti 3d charge transfer, which splits into two peaks (238 and 284 nm) due to the anisotropy of the TiO_2 nanocrystal. A broad peak with λ_{max} = 444 nm can be assigned to the SPR of Ag nanoparticles. On the basis of the data reported by Peng et al.,[56] it is possible to estimate the size of solution-dispersed Ag nanoparticles based on the red shift of the SPR feature. However, an additional red shift of the SPR will occur due to the attachment of the Ag nanoparticles to the TiO_2 surface that has a much higher index of refraction than organic ligands and solvent. Emission spectra (Figure 2d) from TiO_2 nanorods and Ag−TiO_2 HNCs were compared. Using an excitation wavelength of 300 nm, the dispersion of TiO_2 nanorods showed broad, weak luminescence, whereas the dispersion of Ag−TiO_2 HNCs showed no luminescence. Although it is by no means a proof, this observation is consistent with a model in which conduction band electrons produced upon band-gap excitation of TiO_2 are rapidly injected to Ag, thereby quenching luminescence.

Upon adjusting the mole ratio of Ag/TiO_2 in the preparation of HNCs, we observed an effect on the Ag nanoparticle size and number density on the TiO_2 nanorod surface with appreciable effects from the reducing agent. We prepared Ag−TiO_2 HNCs via oleylamine reduction (no 1,2-hexadecanediol) and varied the Ag/TiO_2 ratio. From the TEM

DOI: 10.1021/acsaem.9b01730
ACS Appl. Energy Mater. 2019, 2, 8274−8282

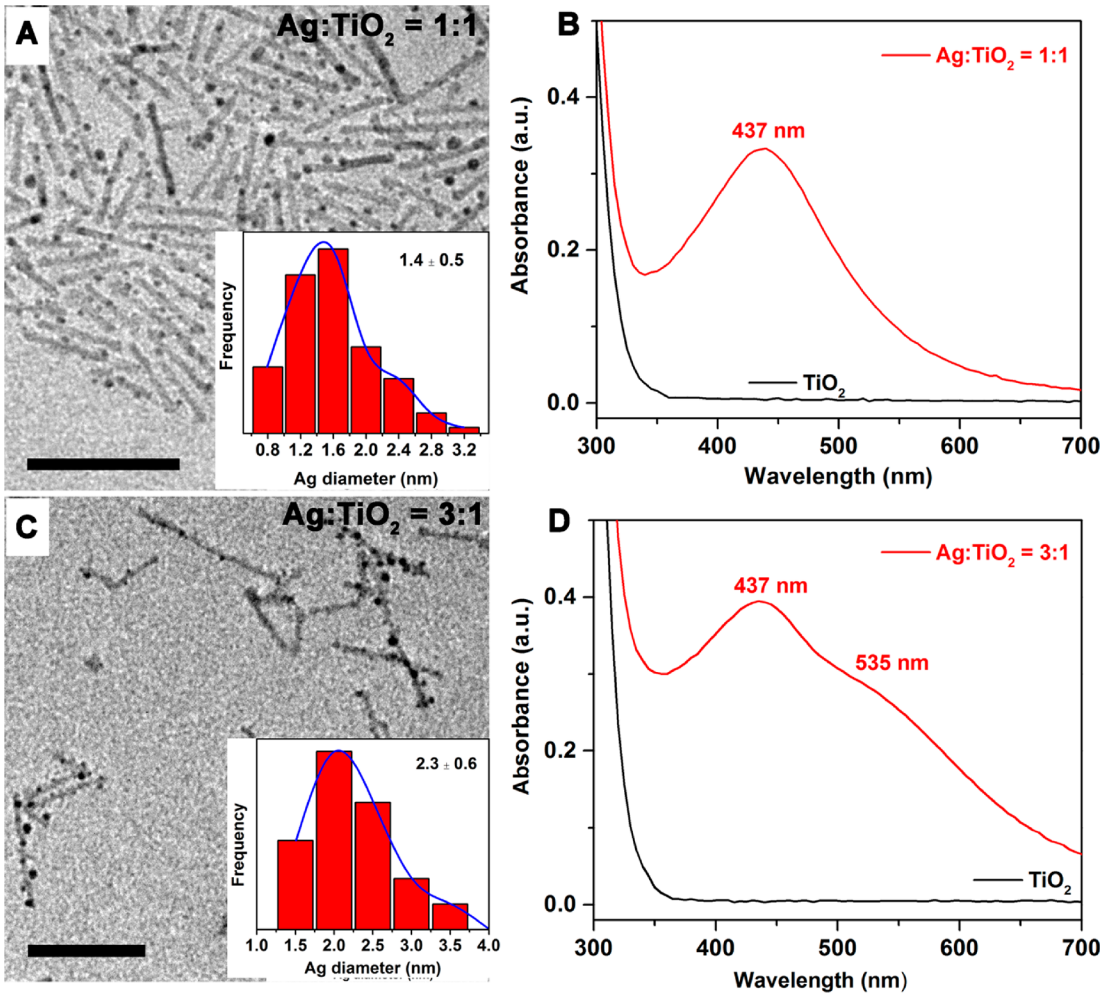

Figure 3. (a) TEM image and (b) UV−visible spectra of Ag−TiO_2 HNCs from oleylamine reduction (Ag/TiO_2 ratio 1:1). (c) TEM image and (d) UV−visible spectra of Ag−TiO_2 HNCs from oleylamine reduction (Ag/TiO_2 ratio 3:1). Scale bar = 50 nm.

data (Figure 3) of Ag−TiO_2 HNCs prepared in which the Ag/TiO_2 ratio was 1:1, the ratio of Ag nanoparticles to TiO_2 nanorods was ∼2.7 (size distribution of Ag nanoparticles was 1.4 ± 0.5 nm), whereas Ag−TiO_2 HNCs prepared from 3:1 ratio Ag/TiO_2 showed ∼5.5 Ag nanoparticles per TiO_2 nanorod (size distribution of Ag nanoparticles was 2.3 ± 0.6 nm). With increasing Ag/TiO_2 ratio, the UV−visible absorbance features from Ag nanoparticles systematically changed (Figure S6). The primary SPR feature grew in intensity with very slight blue-shifting, and the coupled SPR feature grew in intensity with some red-shifting. As the Ag nanoparticle size increases, the primary SPR feature is expected to become more intense and blue-shifted. As the Ag nanoparticle number density on the TiO_2 nanorods increases, we expect more interparticle SPR coupling to occur to give more intense and red-shifted absorbance. Theoretical studies of the electrodynamics of Ag nanoparticle ensembles indicated that strong interparticle dipole coupling contributes a red shift of the SPR.[57] The extreme case of interparticle dipole coupling arises for particles in direct contact, and when aligned on a single axis, these behave as a single elongated particle.

Interestingly, if we adjust the Ag/TiO_2 ratio in the preparation of Ag−TiO_2 HNCs via oleylamine/1,2-hexadecanediol reduction, then we obtain samples with larger Ag nanoparticles and a lower number density of Ag nanoparticles on each TiO_2 nanorod. UV−visible spectra of samples formed from a Ag/TiO_2 ratio of 1:1 and 4:1 from oleylamine/1,2-hexadecanediol reduction show one Ag SPR peak with no additional feature from SPR coupling. TEM data from Ag−TiO_2 HNCs prepared from oleylamine/1,2-hexadecanediol reduction and a 1:1 ratio of Ag/TiO_2 indicate that the Ag nanoparticle diameter is 3.4 ± 0.8 nm and the number density is ∼3.2 Ag nanoparticles per TiO_2 nanorod, whereas the Ag−TiO_2 HNCs prepared from a 4:1 ratio of Ag/TiO_2 have a Ag nanoparticle diameter of 4.0 ± 1.5 nm and a number density of ∼1.9 Ag nanoparticles per TiO_2 nanorod. The data are shown in Figure 4.

Photocatalysis. We assessed the activity of the Ag−TiO_2 HNCs for light-driven hydrogen evolution in methanol/water 1:6 v/v solutions. The Ag−TiO_2 HNCs do not disperse in the aqueous solution, and simply stirring the Ag−TiO_2 HNCs as a slurry is problematic in that the surface sites are blocked due to aggregation and surface ligands. To present the highest possible number of unblocked surface sites for the reaction, we prepared silica-supported Ag−TiO_2 HNCs, followed by mild calcination at 175 °C in a 30 mTorr vacuum oven for 24 h. For comparison, we evaluated Evonik Aeroxide TiO_2 P25 powder, fumed silica, TiO_2 nanorods supported on silica (calcined and uncalcined samples), a powder form of oleic-acid-stabilized TiO_2 nanorods, and a mixture of Ag/SiO_2 and

DOI: 10.1021/acsaem.9b01730
ACS Appl. Energy Mater. 2019, 2, 8274−8282

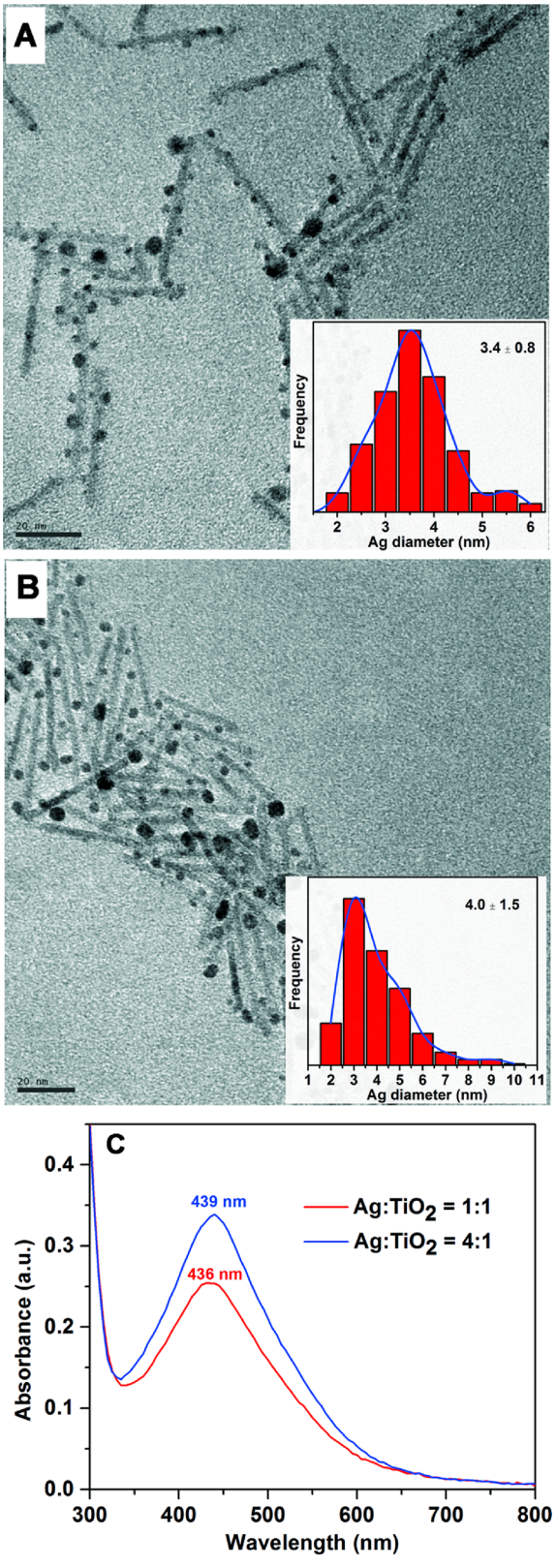

Figure 4. (a) TEM image and Ag size histogram of Ag−TiO_2 HNCs from oleylamine/1,2-hexadecanediol reduction (Ag/TiO_2 ratio 1:1). (b) TEM image and Ag size histogram of Ag−TiO_2 HNCs from oleylamine/1,2-hexadecanediol reduction (Ag/TiO_2 ratio 4:1). (c) UV−visible spectra of Ag−TiO_2 HNCs from oleylamine/1,2-hexadecanediol reduction with varying Ag/TiO_2 ratio. Scale bar = 20 nm.

TiO_2/SiO_2 in which the Ag nanoparticles and TiO_2 nanorods of equal dimensions to the HNCs but spatially separated such that there are no Ag−TiO_2 junctions.

The hydrogen evolution data under unfiltered irradiation from a 150 W Xe arc lamp are presented in Table 1 and Figure 5. The supported Ag−TiO_2 HNCs yield hydrogen at rates up to 12.3 μmol/g catalyst/min. From this rate, we calculate a turnover frequency (TOF = H atoms/site/second in which the site is one surface silver atom) of 1.4×10^{-4} s^{-1}. The apparent quantum yield (AQY) (based on the overlap of the TiO_2 absorbance spectrum and the emission from the Xe arc lamp, $220 < \lambda < 300$ nm) is 0.92%. The average photon flux ($220 < \lambda < 300$ nm) for each surface Ag atom is $\sim 1.5 \times 10^{-2}$ s^{-1}. Considering a hypothetical scenario of 100% light ($220 < \lambda < 300$ nm) absorption by TiO_2, 100% conversion of those incident photons to injected electrons from the TiO_2 conduction band to Ag, and 100% efficiency in proton reduction, the resultant theoretical ceiling for hydrogen evolution is well below those experimentally found for hydrogen evolution on single-crystal Ag electrodes.[58] Therefore, quantum efficiency is not limited by the intrinsic activity of the Ag nanoparticle surface. Rather quantum efficiency must be limited by factors that include the probability of light absorption, the degree of light scattering within the dispersion, the rate of donor oxidation, and the recombination of electrons and holes. Increasing the mass of the catalyst in the reactor leads to diminishing returns on the hydrogen evolution rates that give a lower apparent TOF, which is likely due to the strong light scattering at the front face of the reactor. We carried out the reaction with a UV cutoff filter ($\lambda > 420$ nm transmitted) and found no hydrogen evolution under visible-light illumination. Presumably, the extinction coefficient from the Ag SPR is too low due to the small size of the Ag nanoparticles to give an appreciable charge injection to the TiO_2 conduction band. As noted by Qian et al., the plasmonic photocatalysis on Au−TiO_2 takes place in the presence of large Au nanoparticles with a strong SPR feature.[20] Additionally, the work function of Ag places the Fermi level of the metal close in energy to the conduction band edge of the TiO_2. In this case, any electron transfer from Ag to TiO_2 leads to holes that are weak oxidizers unable to accept electrons from the methanol donor in solution. The addition of formaldehyde as an electron donor similarly gave no hydrogen evolution under visible light. We could rule out the photoreforming of methanol as the source of hydrogen evolution because no carbon dioxide formed during irradiation (Figure S7).

For comparison, fumed silica showed no activity for hydrogen evolution. Silica-supported TiO_2 nanorods yield hydrogen at a rate of 2.00 μmol/g catalyst/min with AQY = 0.13%. Uncalcined TiO_2 nanorods on fumed silica yield hydrogen at a rate of 1.2 μmol/g catalyst/min with AQY = 0.08%. The activity is presumably slower due to presence of oleic acid on the surface of the TiO_2 nanorods that blocks surface titanium sites. Unsupported oleic-acid-stabilized TiO_2 nanorods in powder form yield hydrogen at a rate of 1.46 μmol/g catalyst/min with AQY = 0.09%, which was fairly similar to the result from uncalcined silica-supported TiO_2 nanorods. The Aeroxide P25 powder yields hydrogen at a rate of 2.65 μmol/g catalyst/min with AQY = 0.04%. A mixture of silica-supported TiO_2 nanorods and silica-supported Ag nanoparticles yields hydrogen at a rate of 0.5 μmol/g catalyst/min with AQY = 0.03%. In this sample, there are no contacts between Ag and TiO_2, so there should be no

DOI: 10.1021/acsaem.9b01730
ACS Appl. Energy Mater. 2019, 2, 8274−8282

Table 1. Activity of Photocatalysts for Hydrogen Evolution

catalyst (Ag diameter; no. Ag particles/TiO_2 nanorod)	rate of H_2 evolution (μmol H_2 g cat^{-1} min^{-1})[a]	TOF (10^{-5}/s)	apparent quantum yield %[b]
Ag−TiO_2/SiO_2 (3.4 nm Ag; 3.2 Ag/TiO_2)[c,d]	12.3	14.1[e]	0.92
Ag−TiO_2/SiO_2 (4.0 nm Ag; 1.9 Ag/TiO_2)[c,d]	3.3	3.8[e]	0.25
Ag−TiO_2/SiO_2 (2.1 nm Ag; 4.9 Ag/TiO_2)[c,d]	3.0	3.4[e]	0.22
P25	2.7	5.18	0.04
TiO_2/SiO_2[c]	2.0	0.978	0.13
TiO_2 nanorods	1.5	0.714	0.09
TiO_2/SiO_2 (uncalcined)	1.2	0.587	0.08
mixture Ag/SiO_2 (1.5 wt % Ag) + TiO_2/SiO_2 (1.5 wt % TiO_2)[c]	0.5	0.245	0.03
SiO_2	0	0	0

[a]Rates were calculated based on the mass of active phase (mass Ag + mass TiO_2). [b]AQY based on incident photons absorbed by TiO_2 (λ < 300 nm for TiO_2 nanorods, λ < 400 nm for P25). [c]Calcined ~30 mTorr air at 175 °C for 24 h. [d]3 wt % Ag−TiO_2 HNCs on silica. [e]TOF was calculated based on the number of surface Ag atoms.

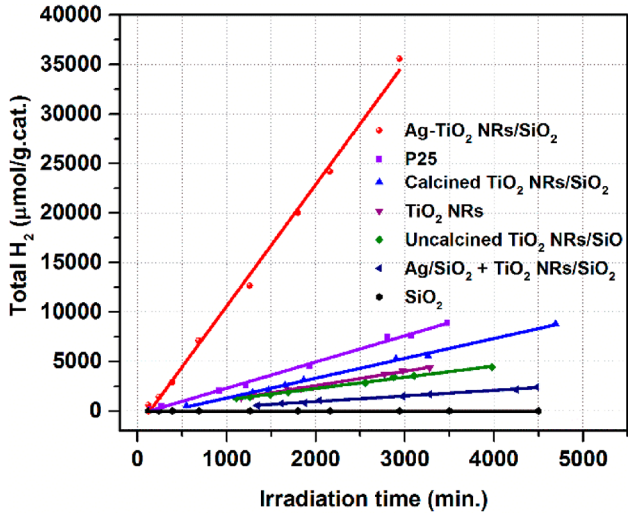

Figure 5. Hydrogen evolution versus time. Samples were irradiated with unfiltered light from 150 W Xe arc lamp.

enhancement in photocatalysis due to the charge injection from the TiO_2 conduction band to Ag. If the activity of the sample is derived from light absorption on TiO_2, then the hydrogen evolution rate should be approximately half that of the silica-supported TiO_2 nanorods. However, the observed activity is substantially less, likely due to light scattering and absorbance from the Ag/SiO_2.

A comparison of Ag−TiO_2 HNCs photocatalysts with different sizes and number densities of Ag particles per TiO_2 nanorods shows that H_2 evolution rates can vary substantially. In the sample showing the highest activity (12.3 μmol H_2 g cat^{-1} min^{-1}), the Ag nanoparticles had an average diameter of 3.4 nm and a number density of ~3.2. A sample with 4.0 nm Ag particles and a number density of ~1.9 showed activity of 3.3 μmol H_2 g cat^{-1} min^{-1}, and a sample with 2.1 nm Ag particles and number density of ~4.9 showed activity of 3.0 μmol H_2 g cat^{-1} min^{-1}. With too few comparisons, it is difficult to delineate the effects of Ag particle size and number density on the TiO_2 surface. Results from the Amirav group show a clear advantage in Pt-decorated CdSe@CdS rods with one cocatalyst site, whereas nanorods multiply decorated with Pt showed greatly lowered activity due to intermediates being distributed over multiple sites.[42] Several groups have reported the size effect of metal cocatalyst on the rates of H_2 evolution on metal−semiconductor photocatalysts. The Amirav group reported rates of H_2 evolution on Pt-decorated CdSe@CdS rods and observed an optimal metal domain size of 5.2 nm. They proposed that increasing the metal domain size facilitates charge separation; however, it also leads to a larger Schottky barrier at the metal−semiconductor interface.[43] The Banin group reported size-controlled Au-CdS HNCs and found an optimal metal domain size.[59] The Idriss group reported H_2 evolution from ethanol on Au/TiO_2 photocatalysts under UV irradiation and observed an optimal size of ~12 nm.[60] In a separate study of M/TiO_2 (M = Pd, Pt, Au) catalysts, the effects of metal loading and particle size on H_2 production from ethanol/water under UV irradiation were compared.[61] The rate of formation of H_2 correlated with the metal work function, but showed a complex dependence on the metal particle size and the number density on the TiO_2 surface. Berr and coworkers studied H_2 evolution from well-defined Pt nanoclusters on CdS nanorods and concluded that electron transfer from the semiconductor to the metal was most effective when the separation between Pt clusters was approximate to the spatial extent of the electronic wave function (5−8 nm in this system).[62] Overall, the size and number density of the cocatalyst on HNCs are important considerations in photocatalyst design.

CONCLUSIONS

The chemical reduction of $AgNO_3$ in the presence of oleic-acid-stabilized anatase TiO_2 nanorods using oleylamine and 1,2-hexadecanediol led to the formation of Ag nanoparticles and Ag−TiO_2 HNCs. The size and number distribution of Ag nanoparticles on the TiO_2 nanorod surface could be tuned based on the selection of the reducing agent and the ratio of Ag/TiO_2 in the synthesis. The average diameter of Ag nanoparticles ranged from ~1.5 to 4.0 nm, and the number densities ranged from ~2 to 5.5 Ag nanoparticles/TiO_2 nanorod. Ag−TiO_2 HNCs with 3.4 nm Ag domains showed the highest activity for H_2 evolution. The silica-supported Ag−TiO_2 HNCs showed ~14× activity compared with silica-supported TiO_2 nanorods. Band-gap excitation of TiO_2, followed by electron injection from TiO_2 to Ag leads to charge separation and hydrogen evolution. However, visible-light excitation of the Ag SPR did not lead to hydrogen evolution. This may be due to multiple factors, such as the low extinction coefficient of the Ag SPR on small Ag nanoparticles, the small energy difference between the TiO_2 conduction band edge and the Ag Fermi level, and the insufficient oxidizing power of Ag holes. Future work could probe the factors that limit visible-light photocatalysis in Ag−TiO_2 HNCs, such as investigating Ag nanostructures with high SPR extinction

DOI: 10.1021/acsaem.9b01730
ACS Appl. Energy Mater. 2019, 2, 8274−8282

coefficients or tuning the Ag Fermi level with different surface ligands.

■ ASSOCIATED CONTENT

Supporting Information

The Supporting Information is available free of charge on the ACS Publications website at DOI: 10.1021/acsaem.9b01730.

Electron micrographs, spectroscopic data, TOF calculations, Rietveld analyses, gas chromatography traces, and EDS data (PDF)

■ AUTHOR INFORMATION

Corresponding Authors

*E-mail: jhoefelm@usd.edu (J.D.H.).
*E-mail: rioux@engr.psu.edu (R.M.R.).

ORCID

Aravind Baride: 0000-0001-7582-1522
Robert M. Rioux: 0000-0002-6019-0032
James D. Hoefelmeyer: 0000-0002-5955-8557

Author Contributions

‖S.J.P.V. and S.M. contributed equally to the work.

Notes

The authors declare no competing financial interest.

■ ACKNOWLEDGMENTS

This work was supported by the National Science Foundation (CHE-0840507, CHE-0722632, CHE-1460872, CHE-1337707, EPS-0903804). C.B. and R.M.R acknowledge funding from the Department of Energy, Office of Basic Energy Sciences, Chemical Sciences, Geosciences, and Biosciences Division, Catalysis Sciences Program under grant number DE-SC0016192.

■ REFERENCES

(1) Bard, A. J.; Fox, M. A. Artificial Photosynthesis: Solar Splitting of Water to Hydrogen and Oxygen. *Acc. Chem. Res.* **1995**, *28*, 141−145.
(2) Gratzel, M. Artificial Photosynthesis: Water Cleavage into Hydrogen and Oxygen by Visible Light. *Acc. Chem. Res.* **1981**, *14*, 376−384.
(3) Osterloh, F. E. Inorganic Materials as Catalysts for Photochemical Splitting of Water. *Chem. Mater.* **2008**, *20*, 35−54.
(4) Lewis, N. S.; Nocera, D. G. Powering the planet: Chemical challenges in solar energy utilization. *Proc. Natl. Acad. Sci. U. S. A.* **2006**, *103*, 15729−15735.
(5) Nocera, D. G. On the future of global energy. *Daedalus* **2006**, *135*, 112−115.
(6) Eisenberg, R.; Nocera, D. G. Preface: Overview of the Forum on Solar and Renewable Energy. *Inorg. Chem.* **2005**, *44*, 6799−6801.
(7) Armaroli, N.; Balzani, V. The Future of Energy Supply: Challenges and Opportunities. *Angew. Chem., Int. Ed.* **2007**, *46*, 52−66.
(8) Bard, A. J. Photoelectrochemistry. *Science* **1980**, *207*, 139−144.
(9) Linsebigler, A. L.; Lu, G.; Yates, J. T., Jr. Photocatalysis on TiO_2 Surfaces: Principles, Mechanisms, and Selected Results. *Chem. Rev.* **1995**, *95*, 735−758.
(10) Kochuveedu, S. T.; Jang, Y. H.; Kim, D. H. A study on the mechanism for the interaction of light with noble metal-metal oxide semiconductor nanostructures for various photophysical applications. *Chem. Soc. Rev.* **2013**, *42*, 8467−8493.
(11) Kelly, K. L.; Coronado, E.; Zhao, L. L.; Schatz, G. C. The Optical Properties of Metal Nanoparticles: The Influence of Size, Shape, and Dielectric Environment. *J. Phys. Chem. B* **2003**, *107*, 668−677.
(12) Noguez, C. Surface Plasmons on Metal Nanoparticles: The Influence of Shape and Physical Environment. *J. Phys. Chem. C* **2007**, *111*, 3806−3819.
(13) Mongin, D.; Shaviv, E.; Maioli, P.; Crut, A.; Banin, U.; Del Fatti, N.; Vallee, F. Ultrafast Photoinduced Charge Separation in Metal-Semiconductor Nanohybrids. *ACS Nano* **2012**, *6*, 7034−7043.
(14) Ma, X.-C.; Dai, Y.; Yu, L.; Huang, B.-B. Energy transfer in plasmonic photocatalytic composites. *Light: Sci. Appl.* **2016**, *5*, No. e16017.
(15) Mubeen, S.; Lee, J.; Singh, N.; Kramer, S.; Stucky, G. D.; Moskovits, M. An autonomous photosynthetic device in which allcharge carriers derive from surface plasmons. *Nat. Nanotechnol.* **2013**, *8*, 247−251.
(16) DuChene, J. S.; Sweeny, B. C.; Johnston-Peck, A. C.; Su, D.; Stach, E. A.; Wei, W. D. Prolonged Hot Electron Dynamics in Plasmonic-Metal/Semiconductor Heterostructures with Implications for Solar Photocatalysis. *Angew. Chem., Int. Ed.* **2014**, *53*, 7887−7891.
(17) Zhang, Y.; He, S.; Guo, W.; Hu, Y.; Huang, J.; Mulcahy, J. R.; Wei, W. D. Surface-Plasmon-Driven Hot Electron Photochemisry. *Chem. Rev.* **2018**, *118*, 2927−2954.
(18) Seh, Z. W.; Liu, S.; Low, M.; Zhang, S.-Y.; Liu, Z.; Mlayah, A.; Han, M.-Y. Janus Au-TiO_2 Photocatalysts with Strong Localization of Plasmonic Near-Fields for Efficient Visible-Light Hydrogen Generation. *Adv. Mater.* **2012**, *24*, 2310−2314.
(19) Lee, K.-S.; El-Sayed, M. A. Gold and Silver Nanoparticles in Sensing and Imaging: Sensitivity of Plasmon Response to Size, Shape, and Metal Composition. *J. Phys. Chem. B* **2006**, *110*, 19220−19225.
(20) Qian, K.; Sweeny, B. C.; Johnston-Peck, A. C.; Niu, W.; Graham, J. O.; DuChene, J. S.; Qiu, J.; Wang, Y.-C.; Engelhard, M. H.; Su, D.; Stach, E. A.; Wei, W. D. Surface Plasmon-Driven Water Reduction: Gold Nanoparticle Size Matters. *J. Am. Chem. Soc.* **2014**, *136*, 9842−9845.
(21) Cozzoli, P. D.; Pellegrino, T.; Manna, L. Synthesis, properties and perspectives of hybrid nanocrystal structures. *Chem. Soc. Rev.* **2006**, *35*, 1195−1208.
(22) Costi, R.; Saunders, A. E.; Banin, U. Colloidal Hybrid Nanostructures: A New Type of Functional Materials. *Angew. Chem., Int. Ed.* **2010**, *49*, 4878−4897.
(23) Donega, C. d. M. Synthesis and properties of colloidal heteronanocrystals. *Chem. Soc. Rev.* **2011**, *40*, 1512−1546.
(24) Buck, M. R.; Schaak, R. E. Emerging Strategies for the Total Synthesis of Inorganic Nanostructures. *Angew. Chem., Int. Ed.* **2013**, *52*, 6154−6178.
(25) Song, H. Metal Hybrid Nanoparticles for Catalytic Organic and Photochemical Transformations. *Acc. Chem. Res.* **2015**, *48*, 491−499.
(26) Fenton, J. L.; Steimle, B. C.; Schaak, R. E. Tunable intraparticle frameworks for creating complex heterostructured nanoparticle libraries. *Science* **2018**, *360*, 513−517.
(27) Borgarello, E.; Kiwi, J.; Pelizzetti, E.; Visca, M.; Gratzel, M. Photochemical cleavage of water by photocatalysis. *Nature* **1981**, *289*, 158−160.
(28) Mokari, T.; Rothenberg, E.; Popov, I.; Costi, R.; Banin, U. Selective Growth of Metal Tips onto Semiconductor Quantum Rods and Tetrapods. *Science* **2004**, *304*, 1787−1790.
(29) Mokari, T.; Sztrum, C. G.; Salant, A.; Rabani, E.; Banin, U. Formation of asymmetric one-sided metal-tipped semiconductor nanocrystal dots and rods. *Nat. Mater.* **2005**, *4*, 855−863.
(30) Habas, S. E.; Yang, P.; Mokari, T. Selective Growth of Metal and Binary Metal Tips on CdS Nanorods. *J. Am. Chem. Soc.* **2008**, *130*, 3294−3295.
(31) Gu, H.; Zheng, R.; Zhang, X.; Xu, B. Facile One-Pot Synthesis of Bifunctional Heterodimers of Nanoparticles: A Conjugate of Quantum Dot and Magnetic Nanoparticles. *J. Am. Chem. Soc.* **2004**, *126*, 5664−5665.
(32) Wu, H.; Chen, O.; Zhuang, J.; Lynch, J.; LaMontagne, D.; Nagaoka, Y.; Cao, Y. C. Formation of Heterodimer Nanocrystals: UO_2/In_2O_3 and $FePt/In_2O_3$. *J. Am. Chem. Soc.* **2011**, *133*, 14327−14337.

DOI: 10.1021/acsaem.9b01730
ACS Appl. Energy Mater. 2019, 2, 8274−8282

(33) Casavola, M.; Grillo, V.; Carlino, E.; Giannini, C.; Gozzo, F.; Fernandez Pinel, E.; Garcia, M. A.; Manna, L.; Cingolani, R.; Cazzoli, P. D.; et al. Topologically Controlled Growth of Magnetic-Metal-Functionalized Semiconductor Oxide Nanorods. *Nano Lett.* **2007**, *7*, 1386−1395.
(34) Shi, W.; Zeng, H.; Sahoo, Y.; Ohulchanskyy, T. Y.; Ding, Y.; Wang, Z. L.; Swihart, M.; Prasad, P. N. A General Approach to Binary and Ternary Hybrid Nanocrystals. *Nano Lett.* **2006**, *6*, 875−881.
(35) Heitsch, A. T.; Hessel, C. M.; Akhavan, V. A.; Korgel, B. A. Colloidal Silicon Nanorod Synthesis. *Nano Lett.* **2009**, *9*, 3042−3047.
(36) Deka, S.; Falqui, A.; Bertoni, G.; Sangregorio, C.; Poneti, G.; Morello, G.; Giorgi, M.; Giannini, C.; Cingolani, R.; Manna, L.; Cozzoli, P. D. Fluorescent Asymmetrically Cobalt-Tipped CdSe@CdS Core@Shell Nanorod Heterostructures Exhibiting Room-Temperature Ferromagnetic Behavior. *J. Am. Chem. Soc.* **2009**, *131*, 12817−12828.
(37) Patra, B. K.; Khilari, S.; Pradhan, D.; Pradhan, N. Hybrid Dot−Disk Au-$CuInS_2$ Nanostructures as Active Photocathode for Efficient Evolution of Hydrogen from Water. *Chem. Mater.* **2016**, *28*, 4358−4366.
(38) Choi, J. Y.; Nam, K. M.; Song, H. Composition effect of alloy semiconductors on Pt-tipped $Zn_{1-x}Cd_xSe$ nanorods for enhanced photocatalytic hydrogen generation. *J. Mater. Chem. A* **2018**, *6*, 16316−16321.
(39) Choi, J. Y.; Jeong, D.; Lee, S. J.; Kang, D.; Kim, S. K.; Nam, K. M.; Song, H. Engineering Reaction Kinetics by Tailoring the Metal Tips of Metal-Semiconductor Nanodumbbells. *Nano Lett.* **2017**, *17*, 5688−5694.
(40) Wachtler, M.; Kalisman, P.; Amirav, L. Charge-Transfer Dynamics in Nanorod Photocatalysts with Bimetallic Metal Tips. *J. Phys. Chem. C* **2016**, *120*, 24491−24497.
(41) Law, M.; Greene, L. E.; Johnson, J. C.; Saykally, R.; Yang, P. Nanowire dye-sensitized solar cells. *Nat. Mater.* **2005**, *4*, 455−459.
(42) Nakibli, Y.; Kalisman, P.; Amirav, L. Less Is More: The Case of Metal Cocatalysts. *J. Phys. Chem. Lett.* **2015**, *6*, 2265−2268.
(43) Nakibli, Y.; Mazal, Y.; Dubi, Y.; Wachtler, M.; Amirav, L. Size Matters: Cocatalyst Size Effect on Charge Transfer and Photocatalytic Activity. *Nano Lett.* **2018**, *18*, 357−364.
(44) Shang, M.; Hou, H.; Gao, F.; Wang, L.; Yang, W. Mesoporous Ag@TiO_2 nanofibers and their photocatalytic activity for hydrogen evolution. *RSC Adv.* **2017**, *7*, 30051−30059.
(45) Alenzi, N.; Liao, W.-S.; Cremer, P. S.; Sanchez-Torres, V.; Wood, T. K.; Ehlig-Economides, C.; Cheng, Z. Photoelectrochemical hydrogen production from water/methanol decomposition using Ag/TiO_2 nanocomposite thin films. *Int. J. Hydrogen Energy* **2010**, *35*, 11768−11775.
(46) Dinh, C.-T.; Nguyen, T.-D.; Kleitz, F.; Do, T.-O. A New Route to Size and Population Control of Silver Clusters on Colloidal TiO_2 Nanocrystals. *ACS Appl. Mater. Interfaces* **2011**, *3*, 2228−2234.
(47) Zhang, Y.; Liu, F.-M. Tunable Optical Properties of Ag−TiO_2 Nanorod Composites Based on Interparticle Plasmon Coupling. *Nano* **2016**, *11*, 1650110.
(48) Yang, S.; Wang, H.; Yu, H.; Zhang, S.; Fang, Y.; Zhang, S.; Peng, F. A facile fabrication of hierarchical Ag nanoparticles-decorated N-TiO_2 with enhanced photocatalytic hydrogen production under solar light. *Int. J. Hydrogen Energy* **2016**, *41*, 3446−3455.
(49) Lu, Q.; Lu, Z.; Lu, Y.; Lv, L.; Ning, Y.; Yu, H.; Hou, Y.; Yin, Y. Photocatalytic Synthesis and Photovoltaic Application of Ag-TiO_2 Nanorod Composites. *Nano Lett.* **2013**, *13*, 5698−5702.
(50) Chen, D.; Chen, Q.; Ge, L.; Yin, L.; Fan, B.; Wang, H.; Lu, H.; Xu, H.; Zhang, R.; Shao, G. Synthesis and Ag-loading-density-dependent photocatalytic activity of Ag@TiO_2 hybrid nanocrystals. *Appl. Surf. Sci.* **2013**, *284*, 921−929.
(51) Hirakawa, T.; Kamat, P. V. Charge Separation and Catalytic Activity of Ag@TiO_2 Core-Shell Composite Clusters under UV-Irradiation. *J. Am. Chem. Soc.* **2005**, *127*, 3928−3934.
(52) Cozzoli, P. D.; Comparelli, R.; Fanizza, E.; Curri, M. L.; Agostiano, A.; Laub, D. Photocatalytic Synthesis of Silver Nanoparticles Stabilized by TiO_2 Nanorods: A Semiconductor/Metal Nanocomposite in Homogeneous Nonpolar Solution. *J. Am. Chem. Soc.* **2004**, *126*, 3868−3879.
(53) Sofianou, M.-V.; Boukos, N.; Vaimakis, T.; Trapalis, C. Decoration of TiO_2 anatase nanoplates with silver nanoparticles on the {101} crystal facets and their photocatalytic behaviour. *Appl. Catal., B* **2014**, *158*−*159*, 91−95.
(54) Joo, J.; Kwon, S. G.; Yu, T.; Cho, M.; Lee, J.; Yoon, J.; Hyeon, T. Large-Scale Synthesis of TiO_2 Nanorods via Nonhydrolytic Sol−Gel Ester Elimination Reaction and Their Application to Photocatalytic Inactivation of E. coli. *J. Phys. Chem. B* **2005**, *109*, 15297−15302.
(55) Naskar, S.; Schlosser, A.; Miethe, J. F.; Steinbach, F.; Feldhoff, A.; Bigall, N. C. Site-Selective Noble Metal Growth on CdSe Nanoplatelets. *Chem. Mater.* **2015**, *27*, 3159−3166.
(56) Peng, S.; McMahon, J. M.; Schatz, G. C.; Gray, S. K.; Sun, Y. Reversing the size-dependence of surface plasmon resonances. *Proc. Natl. Acad. Sci. U. S. A.* **2010**, *107*, 14530−14534. In Figure 3A, authors plot λ_{max} versus diameter, from which we extrapolate a linear relationship over the size range 2.2−5.3 nm with $y = -9.6512x + 463.05$.
(57) Jensen, T.; Kelly, L.; Lazarides, A.; Schatz, G. C. Electrodynamics of Noble Metal Nanoparticles and Nanoparticle Clusters. *J. Cluster Sci.* **1999**, *10*, 295−317.
(58) Eberhardt, D.; Santos, E.; Schmickler, W. Hydrogen evolution on silver single crystal electrodes - first results. *J. Electroanal. Chem.* **1999**, *461*, 76−79.
(59) Ben-Shahar, Y.; Scotognella, F.; Kriegel, I.; Moretti, L.; Cerullo, G.; Rabani, E.; Banin, U. Optimal metal domain size for photocatalysis with hybrid semiconductor-metal nanorods. *Nat. Commun.* **2016**, *7*, 10413.
(60) Murdoch, M.; Waterhouse, G. I. N.; Nadeem, M. A.; Metson, J. B.; Keane, M. A.; Howe, R. F.; Llorca, J.; Idriss, H. The effect of gold loading and particle size on photocatalytic hydrogen production from ethanol over Au/TiO_2 nanoparticles. *Nat. Chem.* **2011**, *3*, 489−492.
(61) Al-Azri, Z. H. N.; Al-Oufi, M.; Chan, A.; Waterhouse, G. I. N.; Idriss, H. Metal Particle Size Effects on the Photocatalytic Hydrogen Ion Reduction. *ACS Catal.* **2019**, *9*, 3946−3958.
(62) Berr, M. J.; Schweinberger, F. F.; Doblinger, M.; Sanwald, K. E.; Wolff, C.; Breimeier, J.; Crampton, A. S.; Ridge, C. J.; Tschurl, M.; Heiz, U.; Jackel, F.; Feldmann, J. Size-Selected Subnanometer Cluster Catalysts on Semiconductor Nanocrystal Films for Atomic Scale Insight into Photocatalysis. *Nano Lett.* **2012**, *12*, 5903−5906.

DOI: 10.1021/acsaem.9b01730
ACS Appl. Energy Mater. 2019, 2, 8274−8282